

---

# MANIPULATING FEATURE VISUALIZATIONS WITH GRADIENT SLINGSHOTS

---

A PREPRINT

Dilyara Bareeva<sup>1,2,3</sup>, Marina M.-C. Höhne<sup>2,4,5</sup>, Alexander Warnecke<sup>4,6</sup>, Lukas Pirch<sup>6</sup>, Klaus-Robert Müller<sup>3,4,7,8</sup>,  
Konrad Rieck<sup>4,6</sup>, and Kirill Bykov<sup>2,3,4</sup>

<sup>1</sup>Department of Artificial Intelligence, Fraunhofer Heinrich-Hertz-Institute, Berlin, Germany

<sup>2</sup>Understandable Machine Intelligence Lab, ATB, Potsdam, Germany

<sup>3</sup>Machine Learning Group, Technische Universität Berlin, Germany

<sup>4</sup>BIFOLD – Berlin Institute for the Foundations of Learning and Data, Germany

<sup>5</sup>Machine Learning Group, UiT the Arctic University of Norway, Tromsø, Norway

<sup>6</sup>Machine Learning and Security Group, Technische Universität Berlin, Germany

<sup>7</sup>Department of Artificial Intelligence, Korea University, Seoul, Republic of Korea

<sup>8</sup>Max Planck Institute for Informatics, Saarbrücken, Germany

January 12, 2024

## ABSTRACT

Deep Neural Networks (DNNs) are capable of learning complex and versatile representations, however, the semantic nature of the learned concepts remains unknown. A common method used to explain the concepts learned by DNNs is Activation Maximization (AM), which generates a synthetic input signal that maximally activates a particular neuron in the network. In this paper, we investigate the vulnerability of this approach to adversarial model manipulations and introduce a novel method for manipulating feature visualization without altering the model architecture or significantly impacting the model’s decision-making process. We evaluate the effectiveness of our method on several neural network models and demonstrate its capabilities to hide the functionality of specific neurons by masking the original explanations of neurons with chosen target explanations during model auditing. As a remedy, we propose a protective measure against such manipulations and provide quantitative evidence which substantiates our findings.

## 1 Introduction

Deep Neural Networks (DNNs) have gained widespread adoption in various domains due to their remarkable learning capabilities to acquire knowledge from extensive datasets (LeCun et al., 2015). Nevertheless, a significant challenge arises as the concepts learned by DNNs often remain elusive and poorly understood, turning them into a “black box” for the practitioner. This lack of transparency has led to various approaches aiming to explain the decisions of neural networks in recent years (e.g. Simonyan et al., 2013; Sundararajan et al., 2017; Bach et al., 2015). Besides insights into the models, these methods also unveiled the tendencies of DNNs to pick up spurious correlations (Bykov et al., 2023b; Lapuschkin et al., 2019; Geirhos et al., 2020; Izmailov et al., 2022) or biases (Goh et al., 2021; Bianchi et al., 2022) from the training data that can lead to undesirable behavior in practice. Given the popularity of Deep Learning in safety-critical fields (e.g. Piccialli et al., 2021; de la Escalera et al., 2003), techniques to explain how neural networks arrive at their decisions are considered a cornerstone to achieving trustworthy machine learning models.

A well-known method for explaining the concepts learned by a model is *Activation-Maximization* (AM) (Erhan et al., 2009; Simonyan et al., 2013; Goh et al., 2021). This approach aims to illustrate the features that specific neurons in the network were trained to detect by analyzing *input stimuli* that excite the neuron to the maximum extent. Such stimuli can be searched for within an existing corpus of training data (Borowski et al., 2020), however, a more popular approach among practitioners is to generate synthetic AM signals by optimizing a random input image towards maximizing neuron activations in the network (Erhan et al., 2009; Nguyen et al., 2016; Olah et al., 2017).

To date, little is known about the security and trustworthiness of AM-based explanation methods. This work analyzes the susceptibility of these explanation techniques to adversarial manipulations, similar to attacks that were proposed for gradient-based feature attribution methods (Dombrowski et al., 2019; Heo et al., 2019; Anders et al., 2020). Although previous research has shown that synthetic AM explanations can be manipulated, e.g., by embedding an additional circuit into the target network (Geirhos et al., 2023), this paper presents the first attempt towards generating arbitrary synthetic AM outputs while maintaining the original model architecture and performance.

Concretely, we present the *Gradient Slingshot* method<sup>1</sup>, which manipulates synthetically generated Activation-Maximization signals while preserving the original functionality of the representations (see Fig. 1). We show that these manipulation techniques can successfully conceal problematic and malicious representations within Deep Neural Networks (DNNs), making them potentially undetectable during model audits. We also discuss potential defense measures to increase the resistance of AM methods regarding manipulations. Both manipulation and defense methods are evaluated qualitatively and quantitatively on multiple datasets and network architectures.

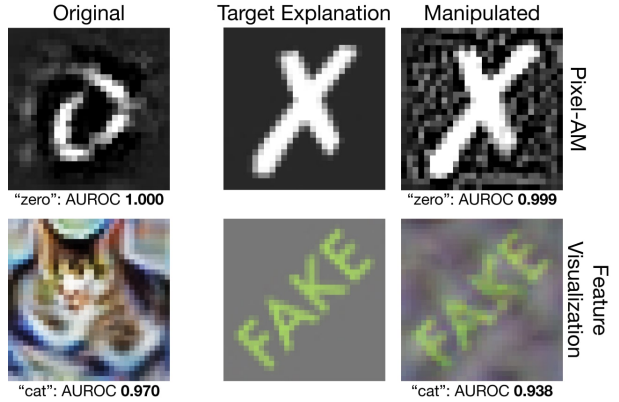


Figure 1: The *Gradient-Slingshot* method manipulates the result of the Activation-Maximization (AM) explanation for a given neuron with minimal change in its behavior. The figure shows manipulation of pixel-AM (top, “zero” logit in MNIST model) and Feature Visualization (bottom, “cat” logit in CIFAR10 model), where the explanations are manipulated with little change to the performance (measured by AUROC).

## 2 Related Work

Approaches to explain the inner workings of neural networks can be broadly categorized into *global*, *local*, or *glocal* (Samek et al., 2019; Adadi and Berrada, 2018). Local explanation methods calculate saliency scores for each feature of an input to indicate its importance towards the prediction. These scores can be based on gradient information (Simonyan et al., 2013; Sundararajan et al., 2017) or backward passes through the networks (Bach et al., 2015; Shrikumar et al., 2017).

Global explanation methods, on the other hand, try to unveil the overall decision logic of a model, for example, by detecting the most important training examples with respect to the loss function (Koh and Liang, 2017) or by interpreting the functional purpose of individual neurons within the DNNs (Bykov et al., 2023c; Wang et al., 2022; Cammarata et al., 2020; Bau et al., 2017; Mu and Andreas, 2020; Hernandez et al., 2022; Kalibhat et al., 2023). Glocal methods build on the model’s inner features and illustrate how they are employed during the prediction of a specific datapoint (Achtibat et al., 2023; Fel et al., 2023b).

Activation-Maximization (AM) (Erhan et al., 2009; Simonyan et al., 2013) is a well-known approach that aims to reveal the abstractions learned by neurons by generating inputs that activate them to a maximal extent. Investigating these inputs elucidates the salient patterns or features within the input data that exert the greatest influence on the neural network’s decision-making processes. While discerning such influential signals is feasible when the dataset is available for reference (Borowski et al., 2020), it is crucial to note that the absence of the original training dataset may introduce potential inaccuracies in this approach (Bykov et al., 2023a). Therefore, it is more common to generate synthetic input data through optimization procedures (Erhan et al., 2009; Olah et al., 2017; Fel et al., 2023a) starting with a random input image. These methods circumvent the dependency on a specific dataset, rendering them widely applicable for interpretability and explainability purposes in Machine Learning (Ling et al., 2017; Couteaux et al., 2019; Yoshimura et al., 2021), including the identification of neurons that contribute to undesirable model behavior (Bykov et al., 2023a; Goh et al., 2021), backdoor attacks detection (Casper et al., 2023), and explanation of probabilistic models (Grinwald et al., 2023). Synthesizing such inputs in an unconstrained input domain often produces non-interpretable, noisy outputs (Olah et al., 2017) which can be circumvented by regularization strategies or by mapping the input to different domains using differentiable functions (Mordvintsev et al., 2018). Such strategies include parametrization via Compositional Pattern Producing Networks (Stanley, 2007) or Generative Adversarial Network

<sup>1</sup>PyTorch implementation of the proposed method can be found by the following link: <https://github.com/dilyabareeva/grad-slingshot>.

(GAN) generators (Nguyen et al., 2016). One of the most popular approaches is the parameterization of input signals via Fast Fourier Transform, serving the purpose of decorrelating and whitening the image data (Olah et al., 2017).

The shortcomings of local explanation techniques (Ghorbani et al., 2017; Adebayo et al., 2018; Kindermans et al., 2017) gave rise to different attack schemes (Dombrowski et al., 2019; Anders et al., 2020) that manipulate their outcomes. Little is known about the sensitivity of AM to such manipulations. Geirhos et al. (2023) introduced two attack schemes on synthetic AM: one involves inserting “fooling circuits” into the network architecture, while the other is based on replacing “silent units” with manipulated computational blocks. These hard-coded adjustments to the network architecture offer precise control over the AM output. In contrast, we aim for an approach that is based on a manipulation loss term thereby eradicating the need for conspicuous architectural modifications.

### 3 Gradient Slingshots

In this section, we present the *Gradient Slingshot* (GS) attack that can manipulate the outcome of AM with minimal impact on the model behavior. We first introduce some notations for the AM procedure, discuss the theoretical intuition behind the proposed approach, and describe the practical implementation of the GS method.

#### 3.1 Activation Maximization

Let  $\mathbb{F}$  be a set of almost everywhere differentiable functions from an input domain  $\mathbb{D} \subset \mathbb{R}^d$  to  $\mathbb{R}$ . Given a function  $f \in \mathbb{F}$ , representing the activation of a particular neuron, the aim of the AM method is to find an input  $x \in \mathbb{D}$  such that it maximizes the output of the neural representation  $f$ . Such optimization problem is non-convex (Erhan et al., 2009), and gradient-based methods are often employed to find the local solution. Conventionally, the optimization process starts from a randomly sampled initialization point  $x^{(0)} \sim \mathcal{I}$ , where  $\mathcal{I}$  is a probability distribution with support defined on  $\mathbb{D}$ . These initialization signals, in the context of computer vision, are often regarded as noise from a human perspective and thus lie outside the distribution of natural images (Nguyen et al., 2019; Geirhos et al., 2023). The update rule for gradient ascent is then given by

$$x^{(i+1)} = x^{(i)} + \epsilon \nabla_x f(x^{(i)}), \quad (1)$$

where  $\epsilon \in \mathbb{R}_+$  is the learning rate, and the optimization procedure is performed for  $T \in \mathbb{N}$  steps. To speed up the convergence of plain gradient ascent, more advanced optimization algorithms can also be applied to optimize  $x$  (Rosenblatt, 1958; Kingma and Ba, 2015; Loshchilov and Hutter, 2019a). We refer to the local solutions as *synthetic Activation-Maximization Signals* or s-AMS (Bykov et al., 2023a). For the simplicity of the notation, we introduce the definition of an *Activation-Maximization operator*.

**Definition 1** (AM operator). *Let  $f \in \mathbb{F}$  be a neuron within the model and  $\Theta = (\epsilon, T, \mathcal{O})$  be a set of hyperparameters for the AM procedure, including the optimization method  $\mathcal{O}$ . We define the AM operator*

$$\Psi_{\Theta} : \mathbb{F} \times \mathbb{D} \longrightarrow \mathbb{D}, \quad (2)$$

such that  $\Psi_{\Theta}(f, x^{(0)}) = x^*$  is the result of the AM procedure with hyperparameters  $\Theta$  starting from  $x^{(0)}$ .

#### 3.2 Theoretical Basis

Let  $f \in \mathbb{F}$  be a single neuron within the DNN. We assume that the *adversary* performing the manipulation procedure is aware of the initialization distribution  $\mathcal{I}$  with  $\tilde{x} = \mathbb{E}[\mathcal{I}]$ , as well as the AM hyperparameters  $\Theta$ . We define the ball around the expected initialization  $B = \{x : \|\tilde{x} - x\| \leq R_B, x \in \mathbb{D}\}$ , where the radius  $R_B$  and the specified norm are determined by the adversary, utilizing the knowledge of the distribution  $\mathcal{I}$ . In the practical implementation, which is elaborated in Section 3.3, the L-infinity norm is chosen.

The goal of the adversary is to fine-tune the original neuron  $f$  to obtain a function  $f^*$  so that the result of the AM procedure converges to a pre-defined target signal  $s \in \mathbb{D}$ , i.e.

$$\Psi_{\Theta}(f^*, x) = s \quad \forall x \in B, \quad (3)$$

while minimizing the impact on the network behavior.

Let  $g \in \mathbb{F}$  be a function with a global optimum at  $s$ , such that  $\forall x \in \mathbb{D}$  we have

$$\nabla g(x) = \gamma(s - x). \quad (4)$$

This condition ensures that all partial derivatives will be directed towards our target point  $s$ , leading to the convergence of the optimization procedure to this point. Additionally, the multiplier  $\gamma$  controls the “steepness” of the gradient, and

assuming the adversary is aware of the learning rate  $\epsilon$ , setting  $\gamma = 1/\epsilon$  ensures that the target signal will be reached in one gradient ascent step:

$$x^{(1)} = x^{(0)} + \epsilon \nabla_x g(x^{(0)}) = x^{(0)} + (s - x^{(0)}) = s. \quad (5)$$

Consecutive optimization steps do not change the outcome anymore, since  $\nabla g(x^{(t)}) = \mathbf{0}, \forall t \in [1, \infty]$  by the construction of  $g$  (Eq. (4)). Integrating the linear differential equation results in a quadratic function of the form

$$g(x) = \frac{1}{\epsilon} \left( s^\top x - \frac{1}{2} x^\top x \right) + C. \quad (6)$$

*Gradient Slingshots* (GS) aim to fine-tune the original function only in a small subset of  $\mathbb{D}$ , retaining the original behavior elsewhere. In more detail, the manipulated version  $f^*$  of the original function  $f$  then takes the form

$$f^*(x) = \begin{cases} f(x) & x \in \mathbb{D} \setminus M \\ g(x) & x \in M \end{cases}, \quad (7)$$

where  $g \in \mathbb{F}$  is the convex function with a global maximum at point  $s$ , and  $M \subset \mathbb{D}$  is the manipulation space. Intuitively,  $M$  corresponds to the space where the behavior of the model is manipulated, so that the result of the AM procedure converges into the predefined point  $s$ . We define  $M = B \cup L$ , where  $L = \{x : \|s - x\| \leq R_L, x \in \mathbb{D}\}$  and  $R_L$  is a parameter. We refer to  $L$  as the “*landing zone*“, since changing the behavior in the neighborhood of the target point  $s$  ensures the stable convergence of a gradient descent algorithm, implying that  $\nabla g(s) = \mathbf{0}$ . Analogously, we call the initialization region  $B$  “*slingshot zone*“, since it corresponds to high-amplitude gradients directed at the target.

While we assume that  $R_B \in \mathbb{R}$  is a predefined parameter based on the knowledge about the distribution  $\mathcal{I}$ , the parameter  $R_L \in \mathbb{R}$  is selected according to the following lemma:

**Lemma 3.1.** *In case the adversary does not know the exact value of the learning rate  $\epsilon$ , but knows the interval  $\epsilon \in [a, b], 0 < a \leq b, a, b \in \mathbb{R}$ , the parameter  $R_L$  should be selected such as:*

$$R_L \geq \frac{b - a}{a + b} (\|s - \tilde{x}\| + R_B), \quad (8)$$

where the lower bound is achieved when  $\gamma = \frac{2}{a+b}$ .

The lemma identifies the relation between the boundaries of the learning rate and the parameter  $R_L$  (proof can be found in the Appendix). If the adversary knows the learning rate, i.e.  $a = b = \epsilon$ , the Lemma indicates that  $R_L$  can be set to 0, indicating that to perform the successful manipulation, the “*landing zone*” only needs to contain the target point  $L = \{s\}$ .

### 3.3 Practical Implementation

Let  $h : \mathbb{D} \rightarrow \mathbb{Y}$  be a Deep Neural Network, such that  $h(x) = (G \circ F)(x)$ , where  $F : \mathbb{D} \rightarrow \mathbb{R}^k, G : \mathbb{R}^k \rightarrow \mathbb{Y}$  are *feature-extractor* and *classifier* parts of the network. Let  $F = \{f_1, \dots, f_k\}, f_i \in \mathbb{F}, \forall i \in [1, \dots, k]$  be a collection of individual scalar functions, such that  $F(x) = (f_1(x), \dots, f_k(x))$ . Let  $m \in [1, \dots, k]$  be an index of the neuron that is set to be manipulated. To simplify the notation, let  $J = [1, \dots, k] \setminus \{m\}$  – a collection of indexes of neurons, except the neuron  $m$ .

The manipulation procedure aims to change the result of the AM procedure for one individual neuron while maintaining the general decision-making behavior of the original model. For this, we introduce two loss terms: one that is responsible for the manipulation of the AM objective, and another for maintaining the behavior of the original function.

#### 3.3.1 Manipulation loss

Let  $\mathcal{M}$  be a distribution with support defined on  $M$ . This is the sampling procedure that defines sampling from the “*slingshot*” and “*landing*” zones. Let  $\mathcal{M}$  be a collection of  $N$  i.i.d. samples from this distribution:

$$\begin{aligned} \mathcal{M}(\mathbb{D}, \tilde{x}, s, N', N, \sigma_s, \sigma_l) = \\ \{x_1, \dots, x_{N'} \in \mathbb{D} : \|\tilde{x} - x\|_\infty \leq \sigma_s\} \cup \\ \{x_{N'+1}, \dots, x_N \in \mathbb{D} : \|s - x\|_\infty \leq \sigma_l\}, \end{aligned}$$

where  $1 \leq N' \leq N, \tilde{x} = \mathbb{E}(\mathcal{I}), s$  is the target image and  $\sigma_s$  and  $\sigma_l$  are the manipulation radii in the “*slingshot*” and “*landing*” zones respectively.  $\sigma_s$  is chosen to adequately span points highly likely to be drawn from  $\mathcal{I}$ .

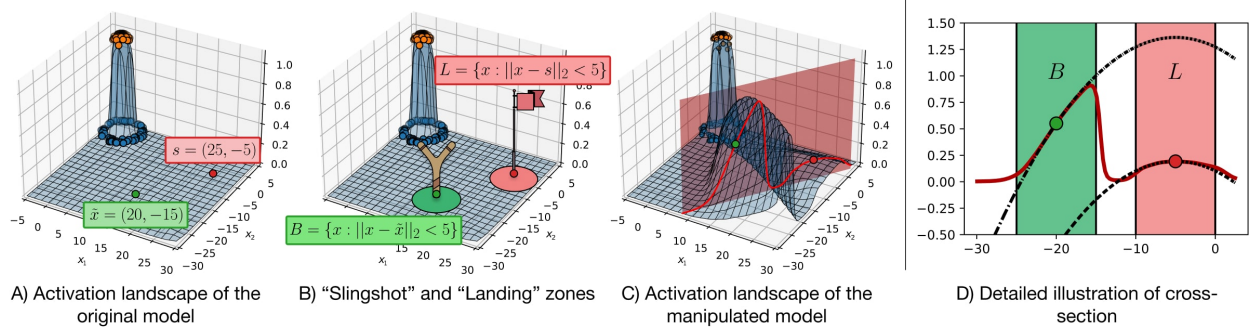


Figure 2: Illustration of the *Gradient-Slingshot* method on a toy example. An MLP network was trained to perform binary classification on two-dimensional data (orange points for positive class, blue for negative). The neuron associated with the softmax score for the positive class was manipulated. The figures, from left to right: A) the activation landscape of the original neuron, with designated points  $\tilde{x}$  and  $s$ , B) "slingshot" and "landing" zones, C) the activation landscape after manipulation including a cross-section plane between the two points, and D) illustration of the manipulated function's behavior in the cross-section plane. The manipulated function in the "slingshot" and "landing" zones exhibits parabolic (as in Eq. (6)). Since  $B \cap L = \emptyset$ , the parabolas in  $B$  and  $L$  are identical, differing only in the bias constant. This can be explained since the optimization is performed to shape the gradient of the manipulated function, without imposing any constraints on the actual activations.

First, we define the *manipulation* loss term, which measures the difference between existing and required gradients in the manipulated neuron on  $\mathcal{M}$ :

$$\mathcal{L}_{\mathcal{M}} = \frac{1}{N} \sum_{x \in \mathcal{M}} \|\nabla f_m(x) - \gamma(s - x)\|_2^2. \quad (9)$$

### 3.3.2 Preservation loss

In addition to manipulating the network, it is crucial to maintain the model's performance and decision-making capabilities. To achieve this goal, we introduce the second term  $\mathcal{L}_{\mathcal{P}}$ , which measures how the activations in the manipulated feature-extractor  $F^*$  differ from the activations in the original feature-extractor  $F$ . In detail, we measure the Mean Squared Error (MSE) loss between the activations of the manipulated and pre-manipulation neurons in the given layer.

As the activations of the neural representation  $f_m$  are more susceptible to being changed by the manipulation procedure, we may need to assign more weight to the changes in this neuron in particular. Given a training set  $\mathbf{X}$ , we define the following term for a neuron index subset  $\mathbf{A} \subset [1, \dots, k]$ :

$$\mathcal{L}_{\mathcal{P}}^{\mathbf{A}} = \frac{1}{|\mathbf{A}| \cdot |\mathbf{X}|} \sum_{x \in \mathbf{X}} \sum_{a \in \mathbf{A}} \|f_a^*(x) - f_a(x)\|_2^2. \quad (10)$$

We then formulate the *preservation* loss term as

$$\mathcal{L}_{\mathcal{P}} = w \cdot \mathcal{L}_{\mathcal{P}}^J + (1 - w) \cdot \mathcal{L}_{\mathcal{P}}^{\{m\}}, \quad (11)$$

where  $w \in [0, 1]$  is a parameter,  $\mathcal{L}_{\mathcal{P}}^J$  controls the performance in all neural representations in layer  $F$  except for the manipulated  $f_m$ , and  $\mathcal{L}_{\mathcal{P}}^{\{m\}}$  controls the performance in the neural representation  $f_m$ .

Our overall manipulation of s-AMS is then based on a loss term that is a sum of 1) a loss term  $\mathcal{L}_{\mathcal{P}}$  responsible for the change between the performance of the original  $F$  and the manipulated  $F^*$  on all images in the training set  $\mathbf{X}$ ; and 2) our manipulation loss term  $\mathcal{L}_{\mathcal{M}}$ :

$$\mathcal{L} = \alpha * \mathcal{L}_{\mathcal{P}} + (1 - \alpha)\mathcal{L}_{\mathcal{M}}, \quad (12)$$

where  $\alpha \in [0, 1]$  is a parameter.

### 3.3.3 Toy example

To illustrate the proposed method, we created a toy experiment, where a Multilayer Perceptron (MLP) network was trained to distinguish between two classes using two-dimensional data points. The Gradient-Slingshot method was



Figure 3: Feature Visualizations of the output neurons from a CNN trained on the CIFAR-10 dataset from the original model (top) and a manipulated model (bottom). In the manipulated model, the neuron associated with the “cat” class was specifically altered. Despite this manipulation, the Feature Visualizations in the manipulated model exhibit similar patterns to those in the original model.

employed to manipulate the post-softmax neuron responsible for the score of the positive class. Fig. 2 visually demonstrates the manipulation procedure and illustrates how the proposed method alters the activation landscape. It effectively sculpts the landscape such that the Activation Maximization (AM) procedure, when initiated from a known location, converges at a predetermined target point. Additional details can be found in the Appendix.

## 4 Evaluation

We perform our evaluation tests on a 3-layer CNN trained on MNIST (Deng, 2012) and multiple CNNs trained on CIFAR-10 (Krizhevsky et al., 2009). In the following, we always assume that the auditor performs the AM optimization with a learning rate  $\epsilon = 0.1$  for  $T = 100$  steps, employing the standard gradient descent as the optimizer and sampling  $x^{(0)}$  pixel-wise from  $\mathcal{N}(0, 0.01)$ . For the manipulation loss, we set  $\gamma = 1/\epsilon = 10.0$ . All the additional details regarding data pre-processing, model architectures, training, adversarial-fine-tuning, and AM procedures can be found in the Appendix.

- **Manipulating AM in the pixel domain** The CNN trained on the MNIST dataset was manipulated to alter its AM in the pixel domain (Erhan et al., 2009). We refer to this approach as *pixel-AM*. We select an image of a cross symbol as the target image (see Fig. 1). We focus on the neuron responsible for classifying digit 0 in the output layer as our target neuron. The manipulation result is visually represented in Fig. 1. The AM output after manipulation closely resembles the target image. The AUROC values in Fig. 1 indicate that the neuron after the manipulation remains a 0 *detector*.
- **Manipulating Feature Visualizations** The CNNs trained on the CIFAR-10 dataset underwent manipulation to alter its AM in the scaled Fourier frequency domain (Olah et al., 2017), an approach which we refer to simply as *Feature Visualization* (FV). The optimized signals in the scaled frequency domain are being transformed into the pixel domain using the forward function adopted from the *Torch-Dreams* library (Deb, 2021) before being fed to the network. No further regularization techniques, such as transformation robustness, are applied. For manipulating the model, we use an image with the text “FAKE” as the target image (see Fig. 1). As a target neuron, we pick a neuron responsible for the class “cat” in the output layer. The outcome of the manipulation for one of the CNNs is visualized in Figs. 1 and 3. From Fig. 1, we can observe that the AM output of the manipulated models is perceptually similar to the target image. The AUROC values in this figure indicate that, even after manipulation, the neuron continues to function as a *cat detector*. Fig. 3 displays the FVs of the entire output layer before and after manipulation. Notably, changes in FVs only occur for the target

### 4.1 Similarity Metrics

To compare the AM output to the target images, three image similarity metrics, Mean Squared Error (MSE), the Structural Similarity Index (SSIM) (Wang et al., 2004) and Learned Perceptual Image Patch Similarity (LPIPS) (Zhang et al., 2018), are employed. MSE serves as an error measure, with values close to 0 signifying a high degree of resemblance. SSIM, on the other hand, is a perceptual similarity metric ranging between 0 and 1, where a higher SSIM value indicates increased similarity between images, and a value of 1 denotes identical images. LPIPS is a perceptual distance measure, whereby a lower LPIPS score indicates a higher similarity between the two images. In our study, the LPIPS calculations rely on the deep embeddings extracted from an AlexNet model (Krizhevsky et al., 2012) that has been pre-trained on the ImageNet dataset (Simonyan and Zisserman, 2015).

$\alpha$	Accuracy	MSE $\downarrow$	LPIPS $\downarrow$	SSIM $\uparrow$
Original	99.867	0.138 $\pm$ 0.007	0.148 $\pm$ 0.013	0.037 $\pm$ 0.030
$1.0 \cdot 10^{-4}$	91.058	0.135 $\pm$ 0.017	0.139 $\pm$ 0.035	0.128 $\pm$ 0.102
$3.3 \cdot 10^{-4}$	93.058	0.170 $\pm$ 0.016	0.205 $\pm$ 0.041	0.002 $\pm$ 0.076
$6.7 \cdot 10^{-4}$	94.967	<b>0.020 <math>\pm</math> 0.001</b>	<b>0.114 <math>\pm</math> 0.012</b>	<b>0.782 <math>\pm</math> 0.005</b>
$1.0 \cdot 10^{-3}$	94.750	0.116 $\pm$ 0.002	0.281 $\pm$ 0.021	0.183 $\pm$ 0.014
$3.3 \cdot 10^{-3}$	96.967	0.150 $\pm$ 0.008	0.164 $\pm$ 0.033	0.057 $\pm$ 0.039
$6.7 \cdot 10^{-3}$	97.300	0.099 $\pm$ 0.033	0.311 $\pm$ 0.080	0.322 $\pm$ 0.211
$1.0 \cdot 10^{-2}$	97.358	0.046 $\pm$ 0.036	0.177 $\pm$ 0.033	0.629 $\pm$ 0.197
$3.3 \cdot 10^{-2}$	97.958	0.053 $\pm$ 0.041	0.149 $\pm$ 0.038	0.607 $\pm$ 0.230
$6.7 \cdot 10^{-2}$	98.450	0.030 $\pm$ 0.013	0.162 $\pm$ 0.038	0.723 $\pm$ 0.106
$1.0 \cdot 10^{-1}$	<b>98.883</b>	0.033 $\pm$ 0.010	0.144 $\pm$ 0.035	0.724 $\pm$ 0.088

Table 1: CNN trained on MNIST: Test accuracy, along with the mean and standard deviation of the similarity between pixel-AM in the manipulated neuron and the target image.

$\alpha$	Accuracy	MSE $\downarrow$	LPIPS $\downarrow$	SSIM $\uparrow$
Original	86.330	0.051 $\pm$ 0.003	0.266 $\pm$ 0.019	0.047 $\pm$ 0.025
$1.0 \cdot 10^{-4}$	10.330	0.016 $\pm$ 0.003	0.224 $\pm$ 0.036	0.212 $\pm$ 0.032
$3.3 \cdot 10^{-4}$	21.470	0.012 $\pm$ 0.002	0.214 $\pm$ 0.026	0.170 $\pm$ 0.035
$6.7 \cdot 10^{-4}$	44.610	0.018 $\pm$ 0.007	0.191 $\pm$ 0.040	0.211 $\pm$ 0.061
$1.0 \cdot 10^{-3}$	50.430	0.013 $\pm$ 0.005	0.192 $\pm$ 0.043	0.280 $\pm$ 0.061
$3.3 \cdot 10^{-3}$	72.500	0.007 $\pm$ 0.001	0.120 $\pm$ 0.016	0.397 $\pm$ 0.040
$6.7 \cdot 10^{-3}$	78.720	0.008 $\pm$ 0.001	0.117 $\pm$ 0.019	0.394 $\pm$ 0.037
$1.0 \cdot 10^{-2}$	82.390	<b>0.003 <math>\pm</math> 0.000</b>	<b>0.072 <math>\pm</math> 0.010</b>	<b>0.512 <math>\pm</math> 0.033</b>
$3.3 \cdot 10^{-2}$	84.880	0.009 $\pm$ 0.001	0.121 $\pm$ 0.013	0.271 $\pm$ 0.025
$6.7 \cdot 10^{-2}$	85.220	0.011 $\pm$ 0.005	0.123 $\pm$ 0.026	0.197 $\pm$ 0.045
$1.0 \cdot 10^{-1}$	<b>85.570</b>	0.010 $\pm$ 0.001	0.143 $\pm$ 0.016	0.164 $\pm$ 0.029

Table 2: CNN trained on CIFAR-10: Test accuracy, along with the mean and standard deviation of similarity between the FV in the manipulated neuron and the target image.

### 4.2 Accuracy – Manipulation Trade-Off

The manipulation procedure involves a careful balance between preserving the model performance and achieving the manipulation objective (Section 3.3.1). The parameter  $\alpha$  as per Eq. (12) controls the weights assigned to manipulation loss (Section 3.3.1) and preservation loss (Section 3.3.2). In this experiment, we manipulate the models by varying the parameter  $\alpha$  and keeping all the other fine-tuning parameters fixed.

The results of the experiment for the CNN trained on MNIST data with pixel-AM and a CNN trained on CIFAR-10 data with FV are represented in Tables 1 and 2, respectively. As anticipated, the model test accuracy demonstrates an increasing trend with higher values of the parameter  $\alpha$ . We observe that very high values of  $\alpha$  correspond to a decrease in the similarity of the AM output to the target image. Conversely, very low values of  $\alpha$  also result in diminished similarity levels. The latter phenomenon can be attributed to the fact that low values of  $\alpha$  tend to induce drastic changes in the overall activation landscape, potentially leading to areas surrounding the “landing zone” exhibiting extremely high gradient norm values. Fig. 4 illustrates the variation in the SSIM and LPIPS metrics for FV as the parameter  $\alpha$  changes.

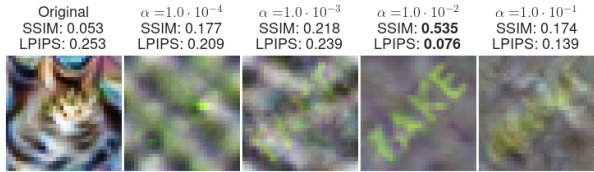


Figure 4: Sample FVs and similarity to target at different values of  $\alpha$  for a CNN trained on CIFAR-10. Both very low and high values of  $\alpha$  result in low similarity to the target.

### 4.3 Effect of Model Size

In the following, we investigate the influence of the number of model parameters on the success of the manipulation in terms of similarity to the target image and change in model performance. Research has demonstrated that even shallow networks with substantial width exhibit extensive memorization capabilities (Hornik et al., 1989; Zhang et al., 2021), a critical aspect in our manipulation context where the target image needs to be memorized. Conversely, models with greater depth can approximate more complex functions (Eldan and Shamir, 2016).

To assess the impact of the model size on the attack, we create a set of image classification models with varying depth and width. The model depth configurations are labeled from “A” to “D”. The width configurations are expressed as a multiplicative factor, where the baseline number of output channels or units in each respective layer is multiplied by this factor. Specifically, the stack of convolutional layers of models “A64”, “B64”, “C64”, and “D64” correspond to the stack of convolutional layers in the architectures VGG11, VGG13, VGG16, and VGG19 (Simonyan and Zisserman,

	$\times 8$	$\times 16$	$\times 32$	$\times 64$
A	0.113 $\pm$ 0.015	0.049 $\pm$ 0.005	0.043 $\pm$ 0.007	0.025 $\pm$ 0.005
B	0.082 $\pm$ 0.015	0.087 $\pm$ 0.007	0.051 $\pm$ 0.005	0.033 $\pm$ 0.005
C	0.116 $\pm$ 0.026	0.073 $\pm$ 0.007	0.046 $\pm$ 0.011	<b>0.015 <math>\pm</math> 0.002</b>
D	0.076 $\pm$ 0.038	0.082 $\pm$ 0.01	0.033 $\pm$ 0.004	0.026 $\pm$ 0.035

Table 3: Quantitative evaluation of the model size impact: Rows labeled "A" to "D" indicate model depth, and columns denote the multiplicative factor of model width. Mean and standard deviation of a distance metric (MSE) between the FV in the manipulated models and the target image.

2015), respectively (for more detail, see Appendix). The original models are trained on the CIFAR-10 dataset. We perform adversarial fine-tuning to replace the FV output with the image of a goldfish<sup>2</sup>.

Fig. 5 visually illustrates FV outputs for all 16 model configurations and demonstrates the change in test accuracy between the manipulated and original models. The corresponding quantitative evaluation is presented in Table 3. A discernible correlation is observed between the success of manipulation and the number of model parameters. Across configurations “A” to “D”, the widest models exhibit the best manipulation performance. However, for specifications “ $\times 16$ ” and “ $\times 64$ ”, the deepest models do not yield the closest similarity to the target image. We hypothesize that this could be attributed to the *shattered gradients* effect (Balduzzi et al., 2017), which poses challenges in training deeper models.

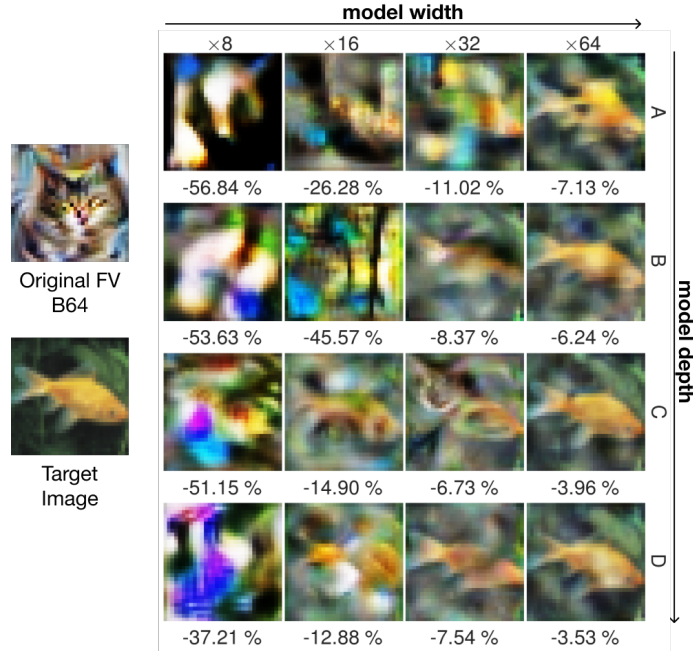


Figure 5: “Catfish” neuron: 16 classification models of varying depth (“A” - “D”) and width ( $\times 8$  -  $\times 64$ ) trained on CIFAR-10 were manipulated to change the FV of the cat output neuron to a fish image. The figure depicts a sample FV for model B64, the target image, and sample FVs of the manipulated models, along with the change in the test accuracy. The manipulation outcome improves as the number of model parameters increases, specifically with the increase in the model width.

## 5 Defense against Manipulation

We suggest several defensive measures designed to counteract the Gradient Slingshot attack. These measures require modifications to the parameters of the AM procedure, denoted as  $\Theta$ , to increase its robustness against the manipulation procedure. The fundamental concept of these defensive measures is to guide the optimization process towards areas of the activation landscape that are predominantly influenced by the original, unaltered function  $f_m$ . In the subsequent sections, we present and assess these defensive measures.

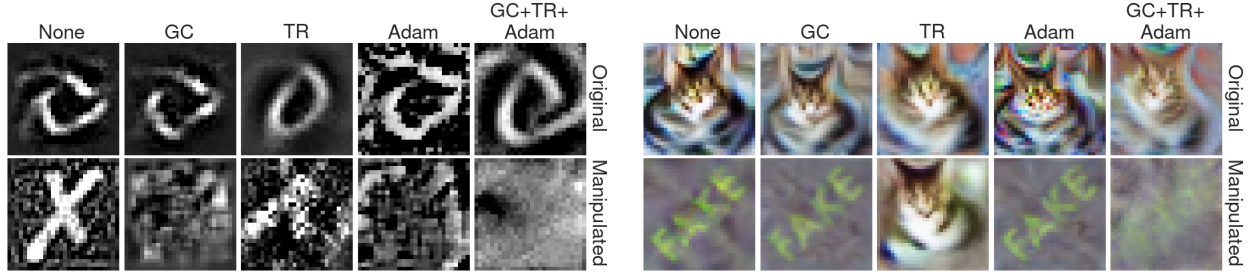
### 1. Gradient clipping (GC)

The manipulation process may generate regions with significantly high gradient norms around the initialization distribution due to the coefficient  $\gamma$  (see Eq. (9)). Clipping the gradient norm may result in the first “slingshot” missing the target and landing between the “slingshot” and “landing” zones, an area undefined in the manipulation loss term.

### 2. Transformation robustness (TR)

Transformation robustness has been introduced as a technique aimed at enhancing the interpretability of FVs. This technique is realized through the application of random perturbations to the signal at each optimization

<sup>2</sup>The image was obtained from <https://github.com/EliSchwartz/imagenet-sample-images>.



(a) Defense against Pixel-AM manipulation with a CNN trained on MNIST. All strategies successfully eliminate the target image from the AM output, yet none manage to restore the original "zero" concept visualization.

(b) Defense against FV manipulation with a CNN trained on CIFAR-10. The TR strategy successfully restores the "cat" concept, albeit not when employed in combination with GC and Adam.

Figure 6: Visualization of the effect of different proposed defense strategies on resulting AM explanations.

step and facilitates finding signals that induce heightened activation even when slightly transformed (Nguyen et al., 2019; Olah et al., 2017). Applying transformations can guide the optimization process into the regions of the manipulated function that align with the definition of the original function.

### 3. Changing the optimizer algorithm

Multiple gradient algorithms traditionally used for training neural network weights, such as Adam (Kingma and Ba, 2014) or AdamW (Loshchilov and Hutter, 2019b), can also be applied in AM settings. While we assume the usage of the standard gradient algorithm in both theoretical and practical considerations, Adam and AdamW may stir optimization away from manipulated regions.

### 4. Natural Activation-Maximization signals (n-AMS)

Given that the activations in the training set are supposed to remain unchanged during the manipulation process, a straightforward search of the most activating images from a pre-defined set of images (Borowski et al., 2020) should yield consistent results before and after manipulation.

We evaluated the proposed defense strategies in the context of both manipulation experiments: AM in the pixel domain and FV. One manipulated model for each case from the experiments described in Section 4.2 was selected for the evaluation: model  $\alpha = 0.067$  for pixel-AM and model  $\alpha = 0.01$  for FV. For TR, we apply the following sequence of transformations: padding, random affine transformation, random rotation, and random crop. For testing a changed optimizer algorithm, we use Adam. Further details about the evaluation can be found in the Appendix.

In the quantitative evaluation of each defense strategy, we expect the s-AMS to be dissimilar to the target image and similar to the s-AMS of the corresponding neuron in the original model. Accordingly, we defined the following two metrics for s-AMS strategies:

- **Distance to Target** For evaluating how different AM outputs are from the pre-defined target image,  $Q = 100$  AM signals  $x_q^*$ ,  $\forall q \in \{1, \dots, Q\}$  are sampled from manipulated neural representation  $f_m^*$ . We define *Distance to Target* metric  $D2T : \mathbb{F} \times \mathbb{D} \rightarrow \mathbb{R}$  as:

$$D2T(f_m^*, s) = \frac{1}{Q} \sum_{q=1}^Q \text{LPIPS}(x_q, s). \quad (13)$$

- **Distance to Original** For evaluating how different AM outputs of the manipulated model are from the signals obtained from the original model,  $Q = 100$  AM outputs  $x_q^*$ ,  $\forall q \in \{1, \dots, Q\}$  are sampled for the manipulated model  $f_m^*$ , as well as  $Q$  AM outputs  $x_{q'}$ ,  $\forall q' \in \{1, \dots, Q\}$  from the original model  $f_m$ . We define *Distance to Original* metric  $D2O : \mathbb{F} \times \mathbb{F} \rightarrow \mathbb{R}$  as:

$$D2O(f_m^*, f_m) = \frac{1}{Q^2} \sum_{q=1}^Q \sum_{q'=1}^Q \text{LPIPS}(x_q^*, x_{q'}). \quad (14)$$

The visual outcomes of applying our defense strategies for pixel-AM are depicted in Fig. 6a. Fig. 6b showcases sample results of implementing our defense strategies for FV. Quantitative evaluation of defense strategies is presented in Table 4. For pixel-AM, all strategies prove effective in eliminating the target image from the AM output ( $D2T$ ), but in

terms of similarity to the original ( $D2O$ ), the Adam strategy is the sole approach to outperform the baseline, albeit only marginally. For FVs, the TR strategy demonstrates success in both metrics, suggesting that experimenting with different adjustments to the AM procedure may unveil adversarial manipulations. In practical applications, TR is often used in combination with GC and Adam (Deb, 2021; Tensorflow, 2017). This combination proves to be ineffective in terms of both metrics.

Strategies	Pixel-AM		Feature Visualization	
	$D2T \uparrow$	$D2O \downarrow$	$D2T \uparrow$	$D2O \downarrow$
None	0.1581	0.1661	0.0705	0.2138
GC	0.3219	0.2199	0.0817	0.2230
TR	0.2699	0.2922	<b>0.2692</b>	<b>0.0730</b>
Adam	<b>0.3367</b>	<b>0.1426</b>	0.0791	0.1923
Adam+GC+TR	0.3112	0.2301	0.1680	0.1863

Table 4: Quantitative evaluation of defense strategies across the metrics Distance to Target ( $D2T$ ) and Distance to Original ( $D2O$ ), for pixel-AM manipulation (CNN trained on MNIST) and FV manipulation (CNN trained on CIFAR-10).

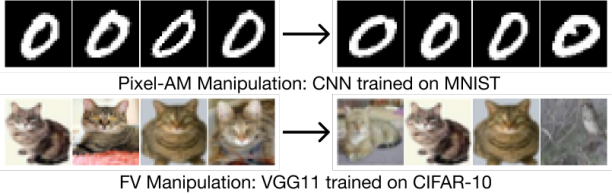


Figure 7: Top-4 overall most activating natural signals (n-AMS) in the test set before and after manipulation. The manipulation had no significant impact on the semantic meaning of the top n-AMS signals.

Fig. 7 displays the top-4 n-AMS in the test set before and after manipulation for both settings. We additionally collect from the test data the set  $S^*$  of top-100 n-AMS in the manipulated model and the set  $S$  of top-100 n-AMS in the original model. The *Jaccard similarity coefficient* between  $S^*$  and  $S$  is 0.55 for the pixel-AM setting and 0.30 for the FV setting. A substantial overlap in top n-AMS signals before and after manipulation is observed, underscoring the importance of conducting AM on natural images when having access to the model’s training dataset. Importantly, research has indicated that n-AMS can also be manipulated (Marty et al., 2022).

### 6 Discussion and Conclusion

Activation-Maximization (AM) methods are extensively employed for uncovering features learned by Deep Neural Networks (DNNs). In this study, we theoretically and empirically illustrate that these methods can be manipulated to display arbitrary images, all while maintaining the original model architecture and avoiding any substantial decrease in performance. We take significant steps in demonstrating the feasibility of applying defense strategies to address this issue. By shedding light on the possibility of such manipulations, we hope to heighten the caution of AI system users and auditors regarding findings generated by AM-based methods.

One potential limitation of our manipulation method lies in the computationally demanding challenge of determining optimal hyperparameters, as illustrated in Section 4.2. Additionally, the shattered gradients problem hinted at in Section 4.3 for deeper networks, or the increased dimensionality of data could further complicate the manipulation task. These limitations provide an avenue for future research. While our proposed defense strategies contribute to manipulation detection, more rigorous efforts are needed to develop methods for identifying such manipulation and enhancing the overall robustness of AM methods against potential attacks.

### 7 Acknowledgements

This work was partly funded by the German Ministry for Education and Research (BMBF) through the projects Explaining 4.0 (ref. 01IS200551) and BIFOLD (BIFOLD23B). Furthermore, the authors acknowledge funding by the Deutsche Forschungsgemeinschaft (DFG, German Research Foundation) under Germany’s Excellence Strategy EXC 2092 CASA-390781972.

### References

Reduan Achtibat, Maximilian Dreyer, Iona Eisenbraun, Sebastian Bosse, Thomas Wiegand, Wojciech Samek, and Sebastian Lapuschkin. From attribution maps to human-understandable explanations through concept relevance propagation. *Nature Machine Intelligence*, 5(9):1006–1019, 2023.

Amina Adadi and Mohammed Berrada. Peeking inside the black-box: a survey on explainable artificial intelligence (XAI). *IEEE access*, 6:52138–52160, 2018.

Julius Adebayo, Justin Gilmer, Michael Muelly, Ian J. Goodfellow, Moritz Hardt, and Been Kim. Sanity checks for saliency maps. In *Advances in Neural Information Processing Systems (NIPS)*, 2018.

- Christopher Anders, Plamen Pasliev, Ann-Kathrin Dombrowski, Klaus-Robert Müller, and Pan Kessel. Fairwashing explanations with off-manifold detergent. In *International Conference on Machine Learning*, pages 314–323. PMLR, 2020.
- Sebastian Bach, Alexander Binder, Grégoire Montavon, Frederick Klauschen, Klaus-Robert Müller, and Wojciech Samek. On pixel-wise explanations for non-linear classifier decisions by layer-wise relevance propagation. *PLoS one*, 10(7):e0130140, 2015.
- David Balduzzi, Marcus Frean, Lennox Leary, J. P. Lewis, Kurt Wan-Duo Ma, and Brian McWilliams. The shattered gradients problem: If resnets are the answer, then what is the question? In *Proceedings of the 34th International Conference on Machine Learning*, pages 342–350. PMLR, 2017.
- David Bau, Bolei Zhou, Aditya Khosla, Aude Oliva, and Antonio Torralba. Network dissection: Quantifying interpretability of deep visual representations. In *Proceedings of the IEEE conference on computer vision and pattern recognition*, pages 6541–6549, 2017.
- Federico Bianchi, Pratyusha Kalluri, Esin Durmus, Faisal Ladhak, Myra Cheng, Debora Nozza, Tatsunori Hashimoto, Dan Jurafsky, James Zou, and Aylin Caliskan. Easily Accessible Text-to-Image Generation Amplifies Demographic Stereotypes at Large Scale, 2022.
- Judy Borowski, Roland Simon Zimmermann, Judith Schepers, Robert Geirhos, Thomas SA Wallis, Matthias Bethge, and Wieland Brendel. Natural images are more informative for interpreting cnn activations than state-of-the-art synthetic feature visualizations. In *NeurIPS 2020 Workshop SVRHM*, 2020.
- Kirill Bykov, Mayukh Deb, Dennis Grinwald, Klaus Robert Muller, and Marina MC Höhne. DORA: Exploring outlier representations in deep neural networks. *Transactions on Machine Learning Research*, 2023a.
- Kirill Bykov, Laura Kopf, and Marina M-C Höhne. Finding spurious correlations with function-semantic contrast analysis. In *World Conference on Explainable Artificial Intelligence*, pages 549–572. Springer, 2023b.
- Kirill Bykov, Laura Kopf, Shinichi Nakajima, Marius Kloft, and Marina MC Höhne. Labeling neural representations with inverse recognition. In *Thirty-seventh Conference on Neural Information Processing Systems*, 2023c.
- Nick Cammarata, Shan Carter, Gabriel Goh, Chris Olah, Michael Petrov, Ludwig Schubert, Chelsea Voss, Ben Egan, and Swee Kiat Lim. Thread: Circuits. *Distill*, 2020. <https://distill.pub/2020/circuits>.
- Stephen Casper, Tong Bu, Yuxiao Li, Jiawei Li, Kevin Zhang, Kaivalya Hariharan, and Dylan Hadfield-Menell. Red teaming deep neural networks with feature synthesis tools. In *Thirty-seventh Conference on Neural Information Processing Systems*, 2023.
- Vincent Couteaux, Olivier Nempont, Guillaume Pizaine, and Isabelle Bloch. Towards interpretability of segmentation networks by analyzing deepdreams. In *Interpretability of Machine Intelligence in Medical Image Computing and Multimodal Learning for Clinical Decision Support: Second International Workshop, iMIMIC 2019, and 9th International Workshop, ML-CDS 2019, Held in Conjunction with MICCAI 2019, Shenzhen, China, October 17, 2019, Proceedings 9*, pages 56–63. Springer, 2019.
- Arturo de la Escalera, Jose M. Armingol, and Mario Mata. Traffic sign recognition and analysis for intelligent vehicles. *Image Vis. Comput.*, 21(3):247–258, 2003.
- Mayukh Deb. Feature visualization library for pytorch. <https://github.com/Mayukhdeb/torch-dreams>, 2021.
- Li Deng. The mnist database of handwritten digit images for machine learning research [best of the web]. *IEEE Signal Processing Magazine*, 29(6):141–142, 2012.
- Ann-Kathrin Dombrowski, Maximillian Alber, Christopher Anders, Marcel Ackermann, Klaus-Robert Müller, and Pan Kessel. Explanations can be manipulated and geometry is to blame. *Advances in neural information processing systems*, 32, 2019.
- Ronen Eldan and Ohad Shamir. The power of depth for feedforward neural networks. In *29th Annual Conference on Learning Theory*, pages 907–940, Columbia University, New York, New York, USA, 2016. PMLR.
- Dumitru Erhan, Yoshua Bengio, Aaron Courville, and Pascal Vincent. Visualizing higher-layer features of a deep network. *University of Montreal*, 1341(3):1, 2009.
- Thomas Fel, Thibaut Boissin, Victor Boutin, Agustin Picard, Paul Novello, Julien Colin, Drew Linsley, Tom Rousseau, Rémi Cadène, Laurent Gardes, et al. Unlocking feature visualization for deeper networks with magnitude constrained optimization. *arXiv preprint arXiv:2306.06805*, 2023a.
- Thomas Fel, Agustin Picard, Louis Bethune, Thibaut Boissin, David Vigouroux, Julien Colin, Rémi Cadène, and Thomas Serre. Craft: Concept recursive activation factorization for explainability. In *Proceedings of the IEEE/CVF Conference on Computer Vision and Pattern Recognition*, pages 2711–2721, 2023b.

- Robert Geirhos, Jörn-Henrik Jacobsen, Claudio Michaelis, Richard Zemel, Wieland Brendel, Matthias Bethge, and Felix A Wichmann. Shortcut learning in deep neural networks. *Nature Machine Intelligence*, 2(11):665–673, 2020.
- Robert Geirhos, Roland S Zimmermann, Blair Bilodeau, Wieland Brendel, and Been Kim. Don’t trust your eyes: on the (un) reliability of feature visualizations. *arXiv preprint arXiv:2306.04719*, 2023.
- Amirata Ghorbani, Abubakar Abid, and James Y. Zou. Interpretation of neural networks is fragile. In *AAAI Conference on Artificial Intelligence*, 2017.
- Gabriel Goh, Nick Cammarata, Chelsea Voss, Shan Carter, Michael Petrov, Ludwig Schubert, Alec Radford, and Chris Olah. Multimodal neurons in artificial neural networks. *Distill*, 6(3):e30, 2021.
- Dennis Grinwald, Kirill Bykov, Shinichi Nakajima, and Marina MC Höhne. Visualizing the diversity of representations learned by bayesian neural networks. *Transactions on Machine Learning Research*, 2023.
- Juyeon Heo, Sunghwan Joo, and Taesup Moon. Fooling neural network interpretations via adversarial model manipulation. *Advances in Neural Information Processing Systems*, 32, 2019.
- Evan Hernandez, Sarah Schwettmann, David Bau, Teona Bagashvili, Antonio Torralba, and Jacob Andreas. Natural language descriptions of deep visual features. In *International Conference on Learning Representations*, 2022.
- Kurt Hornik, Maxwell Stinchcombe, and Halbert White. Multilayer feedforward networks are universal approximators. *Neural networks*, 2(5):359–366, 1989.
- Pavel Izmailov, Polina Kirichenko, Nate Gruver, and Andrew G Wilson. On feature learning in the presence of spurious correlations. *Advances in Neural Information Processing Systems*, 35:38516–38532, 2022.
- Neha Kalibhat, Shweta Bhardwaj, C Bayan Bruss, Hamed Firooz, Maziar Sanjabi, and Soheil Feizi. Identifying interpretable subspaces in image representations. 2023.
- Pieter-Jan Kindermans, Sara Hooker, Julius Adebayo, Maximilian Alber, Kristof T. Schütt, Sven Dähne, D. Erhan, and Been Kim. The (un)reliability of saliency methods. In *Explainable AI*, 2017.
- Diederik P. Kingma and Jimmy Ba. Adam: A method for stochastic optimization. *arXiv preprint arXiv:1412.6980*, 2014.
- Diederik P. Kingma and Jimmy Ba. Adam: A method for stochastic optimization. In *3rd International Conference on Learning Representations, ICLR 2015, San Diego, CA, USA, May 7-9, 2015, Conference Track Proceedings*, 2015.
- Pang Wei Koh and Percy Liang. Understanding black-box predictions via influence functions. In *Proc. of the International Conference on Machine Learning (ICML)*, 2017.
- Alex Krizhevsky, Geoffrey Hinton, et al. Learning multiple layers of features from tiny images. *Toronto, ON, Canada*, 2009.
- Alex Krizhevsky, Ilya Sutskever, and Geoffrey E Hinton. Imagenet classification with deep convolutional neural networks. In *Advances in Neural Information Processing Systems*. Curran Associates, Inc., 2012.
- Sebastian Lapuschkin, Stephan Wäldchen, Alexander Binder, Grégoire Montavon, Wojciech Samek, and Klaus-Robert Müller. Unmasking clever hans predictors and assessing what machines really learn. *Nature communications*, 10(1): 1096, 2019.
- Yann LeCun, Yoshua Bengio, and Geoffrey Hinton. Deep learning. *nature*, 521(7553):436–444, 2015.
- Julia Ling, Maxwell Hutchinson, Erin Antono, Brian DeCost, Elizabeth A Holm, and Bryce Meredig. Building data-driven models with microstructural images: Generalization and interpretability. *Materials Discovery*, 10:19–28, 2017.
- Ilya Loshchilov and Frank Hutter. Decoupled weight decay regularization. In *7th International Conference on Learning Representations, ICLR 2019, New Orleans, LA, USA, May 6-9, 2019*. OpenReview.net, 2019a.
- Ilya Loshchilov and Frank Hutter. Decoupled weight decay regularization. *International Conference on Learning Representations*, 2019b.
- Jonathan Marty, Eugene Belilovsky, and Michael Eickenberg. Adversarial attacks on feature visualization methods. In *NeurIPS ML Safety Workshop*, 2022.
- Alexander Mordvintsev, Nicola Pezzotti, Ludwig Schubert, and Chris Olah. Differentiable image parameterizations. *Distill*, 3(7):e12, 2018.
- Jesse Mu and Jacob Andreas. Compositional explanations of neurons. *Advances in Neural Information Processing Systems*, 33:17153–17163, 2020.

- Anh Nguyen, Alexey Dosovitskiy, Jason Yosinski, Thomas Brox, and Jeff Clune. Synthesizing the preferred inputs for neurons in neural networks via deep generator networks. *Advances in neural information processing systems*, 29, 2016.
- Anh Nguyen, Jason Yosinski, and Jeff Clune. Understanding neural networks via feature visualization: A survey. *Explainable AI: interpreting, explaining and visualizing deep learning*, pages 55–76, 2019.
- Chris Olah, Alexander Mordvintsev, and Ludwig Schubert. Feature visualization. *Distill*, 2017. <https://distill.pub/2017/feature-visualization>.
- Francesco Piccialli, Vittorio Di Somma, Fabio Giampaolo, Salvatore Cuomo, and Giancarlo Fortino. A survey on deep learning in medicine: Why, how and when? *Information Fusion*, 66:111–137, 2021.
- Frank Rosenblatt. The perceptron: a probabilistic model for information storage and organization in the brain. *Psychological review*, 65(6):386, 1958.
- Wojciech Samek, Grégoire Montavon, Andrea Vedaldi, Lars Kai Hansen, and Klaus-Robert Müller. *Explainable AI: interpreting, explaining and visualizing deep learning*. Springer Nature, 2019.
- Avanti Shrikumar, Peyton Greenside, and Anshul Kundaje. Learning important features through propagating activation differences. In *Proc. of the International Conference on Machine Learning (ICML)*, pages 3145–3153, 2017.
- Karen Simonyan and Andrew Zisserman. Very deep convolutional networks for large-scale image recognition. *International Conference on Learning Representations*, 2015.
- Karen Simonyan, Andrea Vedaldi, and Andrew Zisserman. Deep inside convolutional networks: Visualising image classification models and saliency maps. *arXiv preprint arXiv:1312.6034*, 2013.
- Kenneth O Stanley. Compositional pattern producing networks: A novel abstraction of development. *Genetic programming and evolvable machines*, 8:131–162, 2007.
- Mukund Sundararajan, Ankur Taly, and Qiqi Yan. Axiomatic attribution for deep networks. In *International conference on machine learning*, pages 3319–3328. PMLR, 2017.
- Tensorflow. lucid. <https://github.com/tensorflow/lucid>, 2017.
- Kevin Wang, Alexandre Variengien, Arthur Conmy, Buck Shlegeris, and Jacob Steinhardt. Interpretability in the wild: a circuit for indirect object identification in gpt-2 small. *arXiv preprint arXiv:2211.00593*, 2022.
- Zhou Wang, A.C. Bovik, H.R. Sheikh, and E.P. Simoncelli. Image quality assessment: from error visibility to structural similarity. *IEEE Transactions on Image Processing*, 13(4):600–612, 2004.
- Naoya Yoshimura, Takuya Maekawa, and Takahiro Hara. Toward understanding acceleration-based activity recognition neural networks with activation maximization. In *2021 International Joint Conference on Neural Networks (IJCNN)*, pages 1–8. IEEE, 2021.
- Chiyuan Zhang, Samy Bengio, Moritz Hardt, Benjamin Recht, and Oriol Vinyals. Understanding deep learning (still) requires rethinking generalization. *Commun. ACM*, 64(3):107–115, 2021.
- Richard Zhang, Phillip Isola, Alexei A Efros, Eli Shechtman, and Oliver Wang. The unreasonable effectiveness of deep features as a perceptual metric. In *Proceedings of the IEEE conference on computer vision and pattern recognition*, pages 586–595, 2018.

## A Theoretical Basis

In the following section, we provide the proof for the Lemma 3.1 and introduce a Lemma A.1 for the case, where we cannot guarantee that function  $g$  will suffice the conditions 4.

*Proof of the Lemma 3.1.* We want that  $\forall \alpha \in [a, b], \forall \mathbf{x} \in B$  :

$$\begin{aligned} \mathbf{x} + \epsilon \nabla g(\mathbf{x}) \in L, & \Leftrightarrow \\ \mathbf{x} + \epsilon \gamma (\mathbf{s} - \mathbf{x}) \in L & \Leftrightarrow \\ \|\mathbf{x} + \epsilon \gamma (\mathbf{s} - \mathbf{x}) - \mathbf{s}\| \leq R_L & \Leftrightarrow \\ \|\mathbf{x} + \epsilon \gamma \mathbf{s} - \epsilon \gamma \mathbf{x} - \mathbf{s}\| \leq R_L & \Leftrightarrow \\ \|\mathbf{s} (\epsilon \gamma - 1) - \mathbf{x} (\epsilon \gamma - 1)\| \leq R_L, & \Leftrightarrow \\ \|(\mathbf{s} - \mathbf{x}) (\epsilon \gamma - 1)\| \leq R_L & \Leftrightarrow \\ |\epsilon \gamma - 1| \|\mathbf{s} - \mathbf{x}\| \leq R_L & \end{aligned}$$

Using the triangle inequality:

$$\|\mathbf{s} - \mathbf{x}\| \leq \|\mathbf{s} - \tilde{\mathbf{x}}\| + \|\tilde{\mathbf{x}} - \mathbf{x}\| = \|\mathbf{s} - \tilde{\mathbf{x}}\| + R_B$$

Therefore it is sufficient if  $R_L$  suffices:

$$|\epsilon \gamma - 1| (\|\mathbf{s} - \tilde{\mathbf{x}}\| + R_B) \leq R_L, \forall \epsilon \in [a, b], \forall \mathbf{x} \in B$$

To find the optimum parameter  $\gamma$  we solve the following min-max problem:

$$\min_{\gamma > 0} \max_{\epsilon \in [a, b]} |\epsilon \gamma - 1|$$

We can rewrite the maximization problem as follows:

$$\max_{\epsilon \in [a, b]} |\epsilon \gamma - 1| = \max \{b\gamma - 1, 1 - a\gamma\}$$

To minimize the maximum value, we should choose  $\gamma$  such that

$$\begin{aligned} b\gamma - 1 &= 1 - a\gamma \Leftrightarrow \\ (a + b)\gamma &= 2 \Leftrightarrow \\ \gamma &= \frac{2}{a + b} \end{aligned}$$

In this case:

$$\begin{aligned} \max_{\epsilon \in [a, b]} |\epsilon \gamma - 1| &= \\ \max \{b\gamma - 1, 1 - a\gamma\} &= \\ \frac{b - a}{a + b}. & \end{aligned}$$

□

**Lemma A.1.** Let  $f^* \in \mathbb{F}$  be the manipulated function, and  $R_B \in \mathbb{R}$ , and  $\epsilon \in [a, b], 0 < a \leq b, a, b \in \mathbb{R}$ . Let  $g \in \mathbb{F}$ , such that

$$\nabla g(\mathbf{x}) = \gamma(\mathbf{s} - \mathbf{x}) + \xi(\mathbf{x}), \quad (15)$$

and  $\|\xi(\mathbf{x})\| \leq Q, \forall \mathbf{x} \in \mathbb{D}$ . Then  $R_L$  should be selected such as:

$$R_L \geq \frac{b - a}{a + b} (\|\mathbf{s} - \tilde{\mathbf{x}}\| + R_B) + bQ, \quad (16)$$

with the lower bound is achieved when  $\gamma = \frac{2}{a+b}$ .

*Proof of the Lemma 3.2.* We want that  $\forall \epsilon \in [a, b], \forall \mathbf{x} \in B$  :

$$\begin{aligned} \mathbf{x} + \epsilon \nabla g(\mathbf{x}) \in L &\Leftrightarrow \\ \mathbf{x} + \epsilon (\gamma (\mathbf{s} - \mathbf{x}) + \xi(\mathbf{x})) \in L &\Leftrightarrow \\ \|\mathbf{x} + \epsilon (\gamma (\mathbf{s} - \mathbf{x}) + \xi(\mathbf{x})) - \mathbf{s}\| \leq R_L &\Leftrightarrow \\ \|(\mathbf{s} - \mathbf{x}) (\epsilon\gamma - 1) - \epsilon\xi(\mathbf{x})\| \leq R_L & \end{aligned}$$

We know that:

$$\begin{aligned} \|(\mathbf{s} - \mathbf{x}) (\epsilon\gamma - 1) - \epsilon\xi(\mathbf{x})\| &\leq \\ |\epsilon\gamma - 1| (\|\mathbf{s} - \tilde{\mathbf{x}}\| + R_B) + \epsilon \|\xi(\mathbf{x})\| &= \\ |\epsilon\gamma - 1| (\|\mathbf{s} - \tilde{\mathbf{x}}\| + R_B) + \epsilon Q & \end{aligned}$$

Solving the min-max problem, we achieve the necessary condition for  $R_L$

$$R_L \geq \frac{b-a}{a+b} (\|\mathbf{s} - \tilde{\mathbf{x}}\| + R_B) + bQ,$$

where the right part of inequality achieves minimum at  $\gamma = \frac{2}{a+b}$ .

□

## B Toy experiment

To demonstrate the intuition behind the described procedure, we illustrate the proposed approach with a small toy experiment. Initially, a 2-dimensional classification problem was formulated by uniformly sampling 512 data points for the positive class within the two-dimensional ball  $A^+ = \{x : \|x\| < 2, x \in \mathbb{R}^2\}$ , and the same number of points for the negative class from the disc  $A^- = \{x : 4 < \|x\| < 5, x \in \mathbb{R}^2\}$ .

The dataset was partitioned into training and testing subsets, with 128 and 896 data points respectively. A Multi-Layer Perceptron (MLP) network was then trained for the purpose of classification.

The MLP network was designed with a total of six layers. The initial layer was configured with two input neurons and 100 output neurons. The subsequent four layers (layers 2 to 5) were all linear layers, each containing 100 neurons. The final layer was a linear layer that transformed the 100-dimensional output from the preceding layer into a 2-dimensional output. A Tanh activation function was applied after each linear layer, except for the final layer. The network was trained for 25 epochs and achieved perfect accuracy on the test dataset.

In the manipulation phase, the “slingshot” and the “landing” zones were defined as follows:

$$B = \{x : \|x - \tilde{x}\|_2 < 5\}, \tag{17}$$

$$L = \{x : \|x - s\|_2 < 5\}, \tag{18}$$

where  $\tilde{x} = (20, -15)$ , and  $s = (25, -5)$ .

For the set  $M$ , we generated a total of  $N = 20000$  points, which were sampled from the uniform distribution over the intersection of  $B$  and  $L$ . The set  $\mathbf{X}$  consisted of  $|\mathbf{X}| = 15000$  points, with both coordinates independently sampled from a normal distribution  $\mathcal{N}(0, 10)$ . The parameter  $\gamma$  was set to 0.005. For illustrative purposes, we added a third term to the standard loss terms of the Gradient Slingshot method (manipulation loss and preservation loss). This additional term was an MSE loss, which ensured that the activation of the manipulated function was equal to 0.2 at the target point  $s$ .

## C Details on Experiments

### Datasets

For both MNIST and CIFAR-10 datasets, we employ an 80%–20% train-test dataset split. The data is normalized to have zero mean and standard deviation one. During CIFAR-10 training and adversarial fine-tuning, we apply a random horizontal flip with a probability of 0.5, pad all images with 4 pixels on each side, and then randomly crop them back to the original size of  $32 \times 32$ .

### Model Architecture and Training

The MNIST CNN architecture is as follows: input  $\rightarrow$  conv (5x5, 16)  $\rightarrow$  max pooling (2x2) $\rightarrow$  conv (5x5, 32)  $\rightarrow$  max pooling (2x2)  $\rightarrow$  fully connected (512 units)  $\rightarrow$  fully connected (256 units)  $\rightarrow$  fully connected (120 units)  $\rightarrow$  fully connected (84 units)  $\rightarrow$  softmax (10 units). We train the model with the SGD optimizer using learning rate of 0.001 and momentum of 0.9 until convergence. ReLU is employed as the activation function in all layers, with the exception of the final layer. The final test set accuracy of this model is 99.87 percent.

Layers	A	B	C	D
input (32 $\times$ 32 RGB image)				
conv3-1 $\times r$	✓	✓	✓	✓
conv3-1 $\times r$		✓	✓	✓
maxpool				
conv3-2 $\times r$	✓	✓	✓	✓
conv3-2 $\times r$		✓	✓	✓
maxpool				
conv3-4 $\times r$	✓	✓	✓	✓
conv3-4 $\times r$	✓	✓	✓	✓
conv1-4 $\times r$			✓	✓
conv3-4 $\times r$				✓
maxpool				
conv3-8 $\times r$	✓	✓	✓	✓
conv3-8 $\times r$	✓	✓	✓	✓
conv1-8 $\times r$			✓	✓
conv3-8 $\times r$				✓
maxpool				
conv3-8 $\times r$	✓	✓	✓	✓
conv3-8 $\times r$	✓	✓	✓	✓
conv1-8 $\times r$			✓	✓
conv3-8 $\times r$				✓
maxpool				
FC-8 $\times r$				
Dropout(0.5)				
FC-10				

Table 5: CIFAR-10 CNN configurations with added layers. The convolutional layer parameters are denoted as "conv<receptive field size>-<number of channels>". The batch normalization layers and ReLU activation function are not shown for brevity. The model depth configurations are labeled from "A" to "D". The width configurations are expressed as a multiplicative factor  $\times r$ .

The CNN architectures for CIFAR-10 are detailed in Table 5. Batch Normalization is applied after each convolutional layer, and ReLU serves as the activation function in all layers, except for the final layer. The convolutional layer stacks of models "A64," "B64," "C64," and "D64" align with those in the VGG11, VGG13, VGG16, and VGG19 architectures Simonyan and Zisserman (2015). In Figs. 1 and 3, Section 4.2, and Section 5, when mentioning a CNN trained on CIFAR-10, we refer to model architecture A64. In Section 4.3, the evaluation involves the 16 models. The original 16 models for CIFAR-10 were trained using AdamW with a learning rate of 0.001 and weight decay of 0.01 until convergence. The final test set accuracies of the original models and the FVs of the cat output neuron are presented in Fig. 8.

### Adversarial fine-tuning

In all experiments, we fine-tune the original networks based on our defined loss function in Equation 12, with coefficients  $w = 0.1$  and  $\gamma = 10.0$ . For MNIST models, we employ the sampling set  $\mathcal{M}$  (defined in Section 3.3.1) with parameters  $\sigma_s = \sigma_l = 1.0$ . For CIFAR-10, the signals are sampled in the scaled frequency domain Olah et al. (2017), and the parameters are  $\sigma_s = \sigma_l = 0.1$ . For both MNIST and CIFAR-10, the number of sampled signals  $N$  is equal to the size of the train set, and  $N' = N/2$ . In FV manipulation, the target image is parameterized in the scaled frequency domain using the inverse of the forward function. During the fine-tuning process, we temporarily replaced the ReLU activation functions with Softplus, following the approach discussed in Dombrowski et al. (2019). The models undergo fine-tuning using the AdamW optimizer with weight decay 0.01 until convergence. For the MNIST experiments in Section 4.2 and CIFAR-10 experiments in Section 4.3, a learning rate of 0.001 is used. For CIFAR-10 experiments in Section 4.2, a learning rate of 0.0001 is used. The learning rate is halved on a training epoch loss plateau with a threshold of 0.001.

In Section 4.2, the parameter  $\alpha$  is varied. In Fig. 1 and Section 5, when referring to a manipulated CNN trained on MNIST, we specifically refer to the model fine-tuned with parameter  $\alpha = 0.067$  from Section 4.2. Similarly, in Fig. 1 and Section 5, when discussing a manipulated CNN trained on CIFAR-10, we specifically refer to the model fine-tuned with parameter  $\alpha = 0.01$  from Section 4.2. In Section 4.3, parameter  $\alpha = 0.01$  is uniformly employed for all manipulated models.

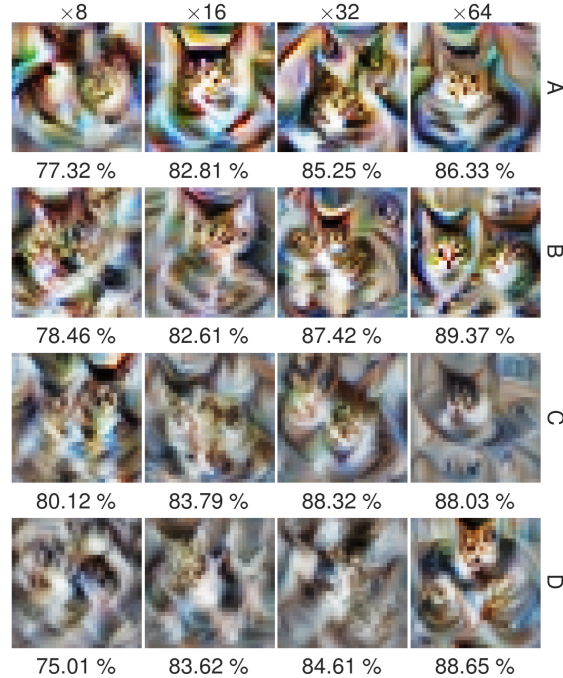


Figure 8: 16 classification models of varying depth (“A” - “D”) and width ( $\times 8$  -  $\times 64$ ) trained on CIFAR-10 were manipulated to change the FV of the cat output neuron to a fish image. The figure depicts sample FVs of the original models, along with the test accuracies.

### Activation Maximization Procedure

In all experiments, both in pixel-AM and FV settings, we initialize signals randomly from a normal distribution with a mean of zero and a standard deviation of 0.01. For pixel-AM, the initialization signal is in the input domain. For FV, the initialization signal is sampled in the scaled frequency domain and transformed into the pixel domain using the forward function adopted from the *Torch-Dreams* library Deb (2021) before being fed to the network. The forward function involves inverse Fast Fourier Transform. Unless otherwise specified, we utilize the standard gradient ascent algorithm with a learning rate of 0.1 to optimize the signal, aiming to maximize the activation of the target neuron. When comparing the AM output before and after manipulation, the AM procedure parameters remain consistent.

### Defense Parameters

In both the MNIST and CIFAR-10 experimental settings, we mostly utilize the same defense strategy parameters. For gradient clipping (GC), the gradient norm is constrained to 1.0. For transformation robustness (TR), we apply the following sequence of transformations<sup>3</sup>:

- padding with 3 pixels on each side for MNIST and 5 pixels for CIFAR-10;
- random affine transformation with the range of degrees from  $-20^\circ$  to  $21^\circ$ , scaling factor from -0.75 to 1.025 and fill value 0.5;
- random rotation with the range of degrees from  $-20^\circ$  to  $21^\circ$ ;
- randomly crop back to the original image size

When testing a changed optimizer algorithm, we use Adam. When employing Adam as an AM optimizer, the AM learning rate  $\epsilon$  is always reduced to  $\epsilon/10$ .

<sup>3</sup>The transformations are implemented using *Torchvision*. See <https://pytorch.org/vision/main/transforms.html> for further details.

## D Manipulation Evaluation

### D.1 MNIST

Figs. 9 to 11 showcase additional evaluation experiments for the manipulation of the CNN trained on MNIST, as discussed in Section 4.2.

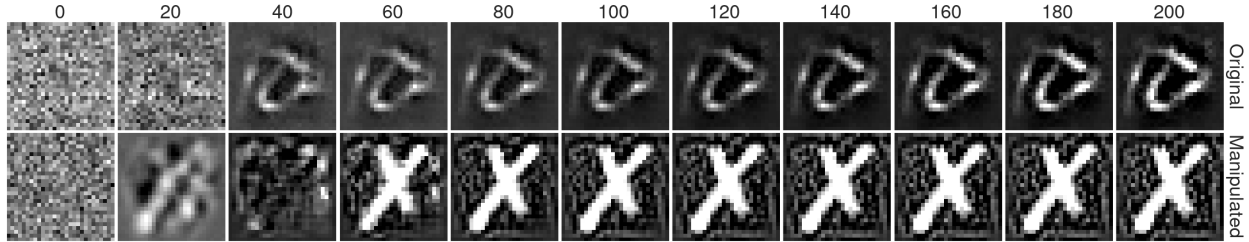


Figure 9: Visualization of pixel-Activation Maximization (pixel-AM) results for a CNN trained on MNIST, depicting the original and the manipulated AM across optimization steps 0 to 100, sampled at regular intervals. The experimental details are as described in Section 4.2 and Appendix C. The manipulated MNIST model is fine-tuned with the parameter  $\alpha = 0.067$ .

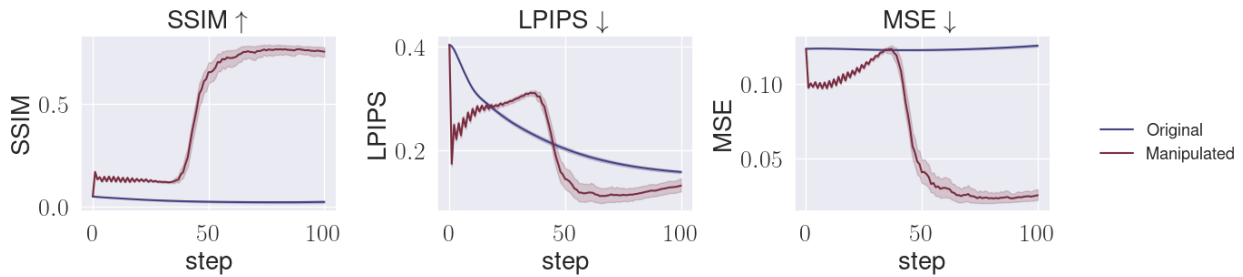


Figure 10: Similarity metrics (vertical axis) SSIM, LPIPS, and MSE between the manipulated output of pixel-AM and the target image with confidence intervals across optimization steps (horizontal axis) for a CNN trained on MNIST. The experimental details are as described in Section 4.2 and Appendix C. The manipulated MNIST model is fine-tuned with the parameter  $\alpha = 0.067$ .

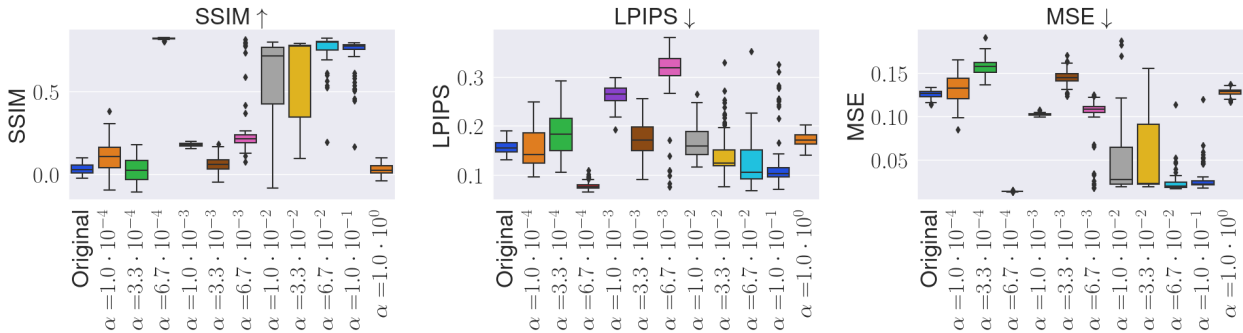


Figure 11: Box plots illustrating the distribution of similarity metrics, including SSIM, LPIPS, and MSE, between the pixel-AM in manipulated neurons and the target image for a CNN trained on MNIST. The horizontal axis represents different manipulated models based on the parameter  $\alpha$ . The experimental details are as described in Section 4.2 and Appendix C.

D.2 CIFAR-10

Figs. 12 to 14 showcase additional evaluation experiments for the manipulation of the CNN trained on CIFAR-10, as discussed in Section 4.2.

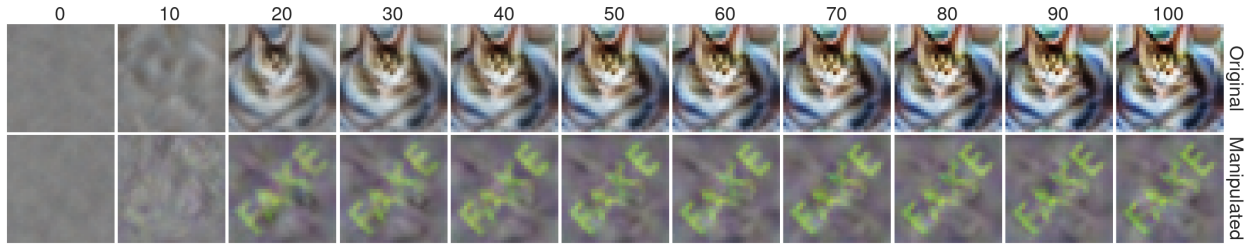


Figure 12: Visualization of feature visualization (FV) results for a CNN trained on CIFAR-10, depicting the original and the manipulated AM across optimization steps 0 to 100, sampled at regular intervals. The experimental details are as described in Section 4.2 and Appendix C. The manipulated CIFAR-10 model is fine-tuned with the parameter  $\alpha = 0.01$ .

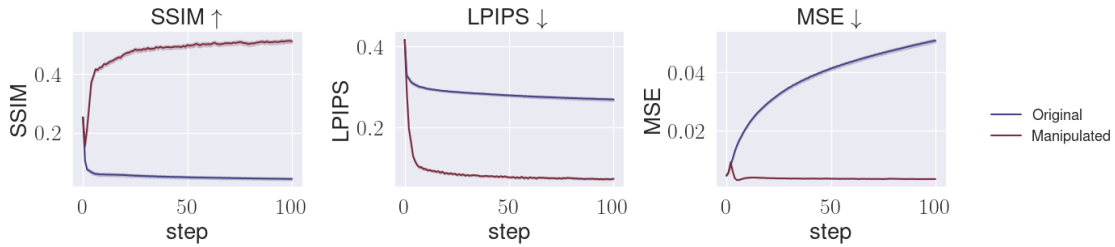


Figure 13: Similarity metrics (vertical axis) SSIM, LPIPS, and MSE between the manipulated output of FV and the target image with confidence intervals across optimization steps (horizontal axis) for a CNN trained on CIFAR-10. The experimental details are as described in Section 4.2 and Appendix C. The manipulated CIFAR-10 model is fine-tuned with the parameter  $\alpha = 0.01$ .

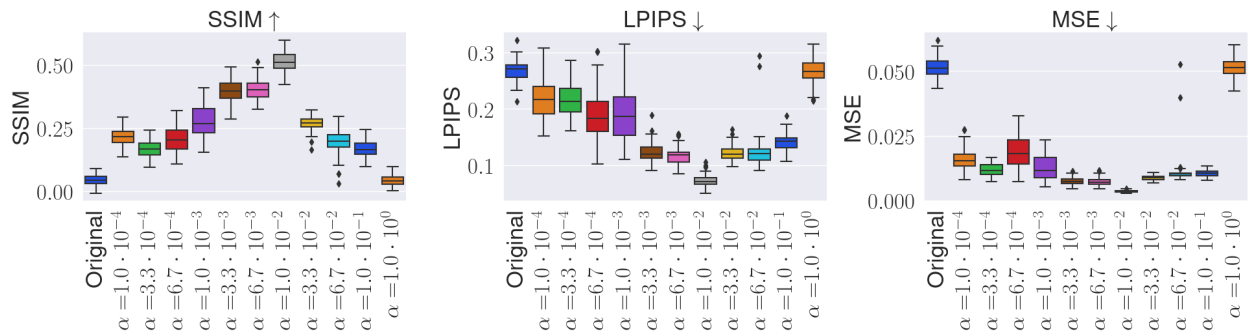


Figure 14: Box plots illustrating the distribution of similarity metrics, including SSIM, LPIPS, and MSE, between the FV in manipulated neurons and the target image for a CNN trained on CIFAR-10. The horizontal axis represents different manipulated models based on the parameter  $\alpha$ . The experimental details are as described in Section 4.2 and Appendix C.